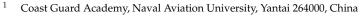*Article*

A UAV Formation Control Method Based on Sliding-Mode Control under Communication Constraints

Qijie Chen [1] , Taoyu Wang [2], Yuqiang Jin [1,*], Yao Wang [1] and Bei Qian [1]

1   Coast Guard Academy, Naval Aviation University, Yantai 264000, China
2   Weapons Academy, Naval Engineering University, Wuhan 430000, China
*   Correspondence: yantaijyq@sohu.com

Abstract: The problem of vision-based fixed-wing UAV formation control under communication limitations and the presence of measurement errors was investigated. In the first part of this paper, the single UAV motion model and the process of estimating the neighboring UAV states using the Extended Kalman Filter are introduced. The second part describes how we designed a sliding mode controller considering the sensor measurement errors and discusses the sufficient conditions for the stability and formation system in the presence of state transfer time delays in the formation. The main motivation of this paper was to develop a hierarchical, globally stable sliding mode controller that could enable the considered vision-based multiple fixed-wing UAVs to achieve and maintain formation in the presence of measurement errors. To this end, the selected problem was first transformed into a state-tracking problem for UAVs in the neighborhood, and then the stability criterion was established using the Lyapunov stability theory. Finally, the effectiveness of the proposed control method was illustrated using three numerical arithmetic examples.

Keywords: UAV; UAV formation; formation control; sliding mode control; time delay system

1. Introduction

In recent years, with the development of technology, UAV formations are able to integrate more sensors compared to single UAVs to achieve diverse tasks in complex mission environments, so UAV formations are widely used in activities such as search [1], reconnaissance and target tracking [2], aerial refueling [3], and cloud computing [4]. In ref. [5], Alsamhi et al. provide a thorough review of the application of UAVs in search. Additionally, considering that although rotary-wing UAVs have the advantages of being mobile and flexible and able to hover at will, but their disadvantages, such as limited load capacity and short flight duration, cannot be ignored, this paper selects fixed-wing UAV formations capable of performing various complex tasks with long flight times as the object of study.

In previous studies, UAV formation control with communication links has become a research topic for researchers because of stable inter-aircraft information transmission, easy implementation, and the ability to adapt to most mission situations to achieve a variety of formation control strategies. According to the control strategy, it can be classified as Leader-Follower [6–8], Virtual Structure [9,10], Behavior-Based [11–13], and Consensus-Based [14,15]. A distributed control method was proposed in [16] to effectively reduce the requirement of the follower UAV speed and achieve formation control under the follower speed no greater than the leader speed limit. Additionally, in [17], to reduce the formation error due to parameter uncertainty, the feedback linearization approach was used to design the formation controller to achieve a zero dynamic error in formation. Unlike the previous two, Zhao et al. in [18] designed controllers with full consideration of UAV input constraints as well as inter-aircraft collision avoidance constraints and implemented simulation experiments in a 3D environment. Kim et al. [19] designed control laws for the

dynamic compensation of UAVs during turns and implemented algorithmic simulations of hardware-in-the-loop. Arumugam et al. in [20] derived sufficient conditions for nonlinear intelligence consistency based on matrix linear inequalities and later in [21] studied multi-intelligence consistency for semi-Markov jump in the perturbed case.

However, in recent years, with the complexity of the mission environment and various types of communication sabotage facilities for UAV formations, it was difficult for UAV formations to form effective communication links within the mission area. Therefore, formation control methods that rely only on visual information transfer are gradually being emphasized by researchers and are widely used in various mission environments. Refs. [22–24] use adaptive primitives to achieve control enhancement without modeling the dynamics and interference, while ref. [25] builds on the former to design the adaptive control of the guiding law line of sight to achieve formation control on a pair of UAVs. A control law based on the inverse height between the optical center of the camera and the feature point was proposed in [26] to achieve formation control under visibility constraints. The ref. [27], on the other hand, designs adaptive control laws for formation control in the absence of a distance state using position navigator velocity and vision-related parameters. To reduce the constraint of information transfer direction, a pilotless formation control method was proposed in [28] and achieved obstacle avoidance and reorganization of the formation. A controller achieved large-scale cluster formation in a measurable error environment, which was presented by Chen et al. in [29] and realized comparative simulations in multiple cases.

Although the above-mentioned article implements vision-based formation control, it makes high demands on the controller design due to the measurement error of the sensor in estimating the state of the leader UAV and the need to form a stable form in a short period. The sliding mode control, on the other hand, is not sensitive to error and has a good control effect, and is widely used by researchers to realize the formation control of UAV formation. To solve the drawbacks of jitter in the sliding mode control method and the difficulty in setting the control gain, adapting the sliding mode control was applied to formation control [30]. The refs. [31,32] integrated sliding-mode controllers into feedback linearization to achieve formation control in the case of unknown leader UAV speed. A bilateral control law using linear quadratic adjustment of the outer loop control and sliding mode control achieved inner loop attitude control and was proposed by Ghamry et al. in [33] to solve the problems of the long computation time of the sliding mode controller and system jitter. To achieve the formation control of multiple aircraft, ref. [34] used a higher-order sliding mode control to achieve the extension of UAV formation. The UAV formation control method is applicable to the model-free case and was proposed in the literature [35], while Mobayen et al. designed two adaptive laws [36] to deal with uncertainties and disturbances with unknown upper bounds, and demonstrated the effectiveness of the algorithm in practical applications. The work in [37], on the other hand, used an integral sliding mode control to achieve the formation control of three UAVs with little change in the speed of the leader.

The above research results show that the sliding mode control algorithm has the advantages of being insensitive to state estimation errors and fast tracking, but there are problems with large initial input values and system jitter. To solve the above problems, this paper adopts the two-layer global stable sliding mode control to design the controller. While ensuring the fast convergence of the system, the sliding mode control input amplitude was limited to ensure that the UAV formation could be controlled under the input limitation and the existence of state estimation delay. The contributions of this paper can be summarized as follows:

(1) The formation control problem of fixed-wing UAVs in an uncommunicated situation was studied. UAVs use only onboard vision sensors to obtain the status of UAVs in the neighborhood and to achieve formation control.

(2)   In this paper, we considered sensor measurements and used Extended Kalman Filtering to reduce errors and designed a sliding mode controller to reduce sensitivity to measurement errors.

(3)   In this paper, the formation control was divided into a two-layer control structure of position control and attitude control, and a suitable Lyapunov function was constructed to prove the system's stability.

(4)   The UAV state transfer delay was considered, the UAV error state equation was given, and a suitable Lyapunov- Krasovskii generalized function was constructed to derive sufficient conditions for the stability of the delayed system, and finally, the obtained theoretical results were illustrated by three numerical simulations.

The rest of the article is outlined below. Section 2 describes the process of estimating the neighborhood UAV state using the Extended Kalman Filter. Section 3 describes the controller development process and sufficient conditions for system stability in the presence of time-delayed states. Section 4 provides numerical simulations to determine the effectiveness of the proposed control method. Finally, then Section 5 gives conclusions.

2. Extended Kalman Filter-Based State Estimation

2.1. Equation of Motion for Single Machine

In order to introduce the UAV formation movement and modeling process, we introduced three coordinate frames I, V_i, and L_i as the inertial coordinate frame, the follower velocity frame of the UAV i, and the line of sight frame. The origin of the follower velocity frame and the line of sight frame is the mass point of the UAV. The relative relationship between the coordinate frames is shown in Figure 1.
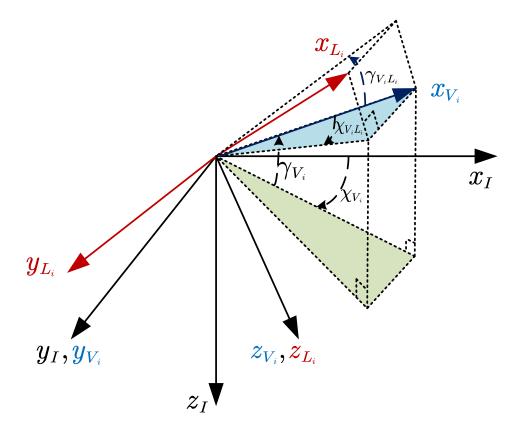

Figure 1. Coordinate frames.

The inter–aircraft relative relationship diagram (shown in Figure 2) can be obtained from Figure 1, where l_{ij}, χ_{ij}, and γ_{ij} are the relative distance, relative yaw angle, and relative pitch angle between the follower and the leader UAV in its neighborhood.
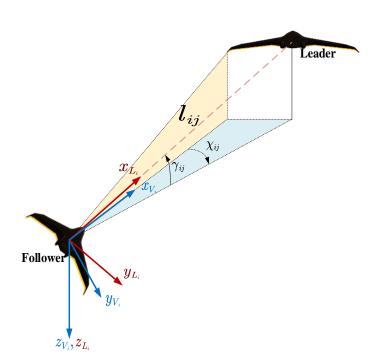
Figure 2. The relative kinematics of the leader-follower.

From [29], the equation of the state of motion of a single UAV is given by:

$$
\dot{x}_i = \begin{bmatrix} \dot{x}_i \\ \dot{y}_i \\ \dot{z}_i \\ \dot{v}_i \\ \dot{\chi}_i \\ \dot{\gamma}_i \end{bmatrix} = \begin{bmatrix} v_i \cos \gamma_i \cos \chi_i \\ v_i \cos \gamma_i \sin \chi_i \\ -v_i \sin \gamma_i \\ a_{xi} \\ a_{zi}/v_i \\ -a_{yi}/v_i \end{bmatrix}
\tag{1}
$$

where: $\boldsymbol{a}_i = \begin{bmatrix} a_{xi}^{V_i} & a_{yi}^{V_i} & a_{zi}^{V_i} \end{bmatrix}^T \in \mathbb{R}^3$ is the UAV control input. Considering the actual flight of the UAV, the input is not able to be chosen arbitrarily, considering the actual state of the UAV, and the input is restricted to a certain action area. Therefore, in this paper, we assumed that the UAV input satisfied:

$$
\boldsymbol{a}_i = \begin{bmatrix} |a_{xi}| \\ |a_{yi}| \\ |a_{zi}| \end{bmatrix} \leq \begin{bmatrix} a_{x\max} \\ a_{y\max} \\ a_{z\max} \end{bmatrix}
\tag{2}
$$

$\begin{bmatrix} a_{x\max} & a_{y\max} & a_{z\max} \end{bmatrix}^T$ in Equation (2) are known constants. The position error between the leader UAV and the follower UAV can be expressed as:

$$
\boldsymbol{e_x} = \begin{bmatrix} e_x \\ e_y \\ e_z \end{bmatrix} = \begin{bmatrix} x_i - x_l \\ y_i - y_l \\ z_i - z_l \end{bmatrix}
\tag{3}
$$

2.2. Leader UAV Status Estimation

In this paper, considering the measurement error in the binocular camera, this paper used the Extended Kalman Filter to estimate the state of the leader UAV. The Extended Kalman Filter for the continuous measurement of the UAV state equation can be expressed as:

$$
\boldsymbol{\Psi}_l(k+1) = \boldsymbol{A}\boldsymbol{\Psi}_l(k) + \boldsymbol{w}(k)
\tag{4}
$$

$$z(k) = H(\mathbf{\Psi}_l(k) - \mathbf{\Psi}_i(k)) + v(k) \tag{5}$$

where, $\mathbf{\Psi}_i(k) = \begin{bmatrix} x_i & y_i & z_i & v_{xi} & v_{yi} & v_{zi} \end{bmatrix}$ is the position and velocity state vector of Leader UAV. $z(k) = \begin{bmatrix} l_{ij} & \chi_{ij} & \gamma_{ij} \end{bmatrix}^T$ is the relative information vector between the navigator and the follower where:

$$A = \begin{bmatrix} 1 & 0 & 0 & T & 0 & 0 \\ 0 & 1 & 0 & 0 & T & 0 \\ 0 & 0 & 1 & 0 & 0 & T \\ 0 & 0 & 0 & 1 & 0 & 0 \\ 0 & 0 & 0 & 0 & 1 & 0 \\ 0 & 0 & 0 & 0 & 0 & 1 \end{bmatrix}, H = \begin{bmatrix} \frac{\partial l_{ij}}{x_i} & \frac{\partial l_{ij}}{y_i} & \frac{\partial l_{ij}}{z_i} & \frac{\partial l_{ij}}{v_{xi}} & \frac{\partial l_{ij}}{v_{yi}} & \frac{\partial l_{ij}}{v_{zi}} \\ \frac{\partial \chi_{ij}}{x_i} & \frac{\partial \chi_{ij}}{y_i} & \frac{\partial \chi_{ij}}{z_i} & \frac{\partial \chi_{ij}}{v_{xi}} & \frac{\partial \chi_{ij}}{v_{yi}} & \frac{\partial \chi_{ij}}{v_{zi}} \\ \frac{\partial \gamma_{ij}}{x_i} & \frac{\partial \gamma_{ij}}{y_i} & \frac{\partial \gamma_{ij}}{z_i} & \frac{\partial \gamma_{ij}}{v_{xi}} & \frac{\partial \gamma_{ij}}{v_{yi}} & \frac{\partial \gamma_{ij}}{v_{zi}} \end{bmatrix}$$

The estimation process of the Extended Kalman Filter can be divided into the following estimation parts as well as the gain update part,

$$\begin{aligned} \hat{\mathbf{\Psi}}_l(k+1|k) &= A\hat{\mathbf{\Psi}}_l(k|k) \\ P(k+1|k) &= AP(k|k)A^T + Q(k) \end{aligned} \tag{6}$$

where $\hat{\mathbf{\Psi}}_l$ is the leader state estimation vector, P is the covariance matrix of the state errors, and is the covariance matrix of noise due to sensor errors in the state variables. After obtaining the state estimation vector, the state estimation vector was corrected by the following equation, and the Kalman gain was updated by Equation (8).

$$\begin{aligned} \hat{\mathbf{\Psi}}_l(k+1|k+1) &= \hat{\mathbf{\Psi}}_l(k+1|k) + K(k)[z(k) - H(\mathbf{\Psi}_l(k+1|k) - \mathbf{\Psi}_i(k))] \\ P(k+1|k) &= P(k+1|k) - K(k)BP(k+1|k) \end{aligned} \tag{7}$$

$$K(k) = P(k+1|k)B^T \left(BP(k+1|k)B^T + R(k) \right)^{-1} \tag{8}$$

where R is the measurement noise caused by the measurement and B is the output matrix, which can be expressed in the following form.

$$B = I_{6 \times 6} \tag{9}$$

By applying the extended Kalman filter, the leader state vector $\mathbf{\Psi}_l(k) = \begin{bmatrix} x_l & y_l & z_l & v_{xl} & v_{yl} & v_{zl} \end{bmatrix}$ could be obtained, and the leader state could be obtained by calculating:

$$p_l = \begin{bmatrix} x \\ y \\ z \end{bmatrix}, v_l = \begin{bmatrix} \dot{x} \\ \dot{y} \\ \dot{z} \end{bmatrix} = \begin{bmatrix} v_{xl} \\ v_{yl} \\ v_{zl} \end{bmatrix} \tag{10}$$

Through the above state estimation for UAVs in the neighborhood, the follower UAV can obtain the reference state information of UAVs in the neighborhood.

3. Controller Design

The controller designed in this paper controlled the inner and outer loops of the UAV separately to realize the position control of the outer loop and the attitude control of the inner loop, respectively. The ideal state of the inner-loop control was generated while realizing the outer-loop control, which then passed to the inner-loop, and then the controller design of the inner-loop realized the tracking of the passed signal and finally realized the closed-loop control of the whole system. In this paper, UAV_l was used to represent the reference UAV in the neighborhood of UAV_i. The flow chart of the algorithm is shown in Figure 3.
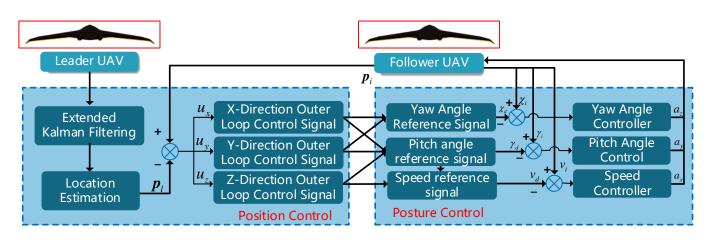
Figure 3. Schematic diagram of algorithm principle.

One note here: in the controller design of this paper, we will use the following second-order differential controller to implement the derivation of the intermediate ideal state differential generated by the outer loop.

$$\begin{cases} \dot{x}_1 = x_2 \\ \dot{x}_2 = -2R^2(x_1 - n(t)) - Rx_x \\ y = x_x \end{cases} \tag{11}$$

where $n(t)$ is the input signal and is the component to be differentiated, x_1 achieves the tracking of the signal, and x_2 is an estimate of the first-order derivative of the signal $n(t)$. The initial states of x_1 and x_2 are defined as $x_1(0) = 0, x_2(0) = 0$.

3.1. Controller Design

For the UAV to have a smooth trajectory, this also meant that it needed to be a smooth curve to make the input to the UAV continuous in the 3D environment. From Equation (1), we obtained:

$$v_i = \sqrt{\dot{x}_i^2(t) + \dot{y}_i^2(t) + \dot{z}_i^2(t)} \tag{12}$$

$$\chi_i = -\arctan^{-1}\left(\frac{\dot{y}(t)}{\dot{x}(t)}\right) \tag{13}$$

$$\gamma_i = -\arctan^{-1}\left(\frac{\dot{z}(t)}{\sqrt{\dot{x}^2(t) + \dot{y}^2(t)}}\right) \tag{14}$$

Together with Equations (1), (12)–(14), we can obtain the acceleration of the UAV as:

$$a_{xi} = \dot{v}_i = \frac{\dot{x}_i(t)\ddot{x}_i(t) + \dot{y}_i(t)\ddot{y}_i(t) + \dot{z}_i(t)\ddot{z}_i(t)}{\sqrt{\dot{x}_i^2(t) + \dot{y}_i^2(t) + \dot{z}_i^2(t)}} \tag{15}$$

$$a_{yi} = v_i\dot{\gamma}_i = -\frac{\ddot{z}_i(t)\left[\dot{x}_i^2(t) + \dot{y}_i^2(t)\right] - \dot{z}_i(t)\left[\dot{x}_i(t)\ddot{x}_i(t) + \dot{y}_i(t)\ddot{y}_i(t)\right]}{\sqrt{\dot{x}_i^2(t) + \dot{y}_i^2(t) + \dot{z}_i^2(t)}\sqrt{\dot{x}_i^2(t) + \dot{y}_i^2(t)}} \tag{16}$$

$$a_{zi} = v_i\dot{\chi}_i = \sqrt{\dot{x}_i^2(t) + \dot{y}_i^2(t) + \dot{z}_i^2(t)}\frac{\dot{x}_i(t)\ddot{y}_i(t) - \ddot{x}_i(t)\dot{y}_i(t)}{\dot{x}_i^2(t) + \dot{y}_i^2(t)} \tag{17}$$

From the above equation, the UAVs could achieve formation control in the case of multiple UAVs with smooth paths under continuous trajectories. It was assumed that the desired trajectory of the UAV in the 3D environment was:

$$\begin{bmatrix} x_d(t) \\ y_d(t) \\ z_d(t) \end{bmatrix} = \begin{bmatrix} f_d(t) \\ g_d(x_d(t)) \\ h_d(x_d(t)) \end{bmatrix} \tag{18}$$

Considering that the UAVs' input is constrained, the following assumptions were made on the trajectory function.

$$\left| \frac{dg_d(x)}{dx} \right| \le \lambda_1, \left| \frac{d^2 g_d(x)}{d^2 x} \right| \le \lambda_2, \forall x \in [0, \infty) \tag{19}$$

$$\left| \frac{dh_d(x)}{dx} \right| \le \mu_1, \left| \frac{d^2 h_d(x)}{d^2 x} \right| \le \mu_2, \forall x \in [0, \infty) \tag{20}$$

where $\lambda_1, \lambda_2, \mu_1, \mu_2$ is the determining constant. By substituting Equation (18) into Equations (15)–(17), which yielded:

$$a_{xi} = \frac{\dot{f}_d^2(t)\left(\frac{d^2 g_d(x)}{d^2 x} + \frac{d^2 h_d(x)}{d^2 x} \right) + \ddot{f}_d(t)\left(\frac{dg_d(x)}{dx} + \frac{dh_d(x)}{dx} \right)}{\sqrt{1 + \left(\frac{dg_d(x)}{dx} \right)^2 + \left(\frac{dh_d(x)}{dx} \right)^2}} \tag{21}$$

$$a_{yi} = -\dot{f}_d(t)\frac{\frac{dh_d(x)}{dx}\left(1 + \left(\frac{dg_d(x)}{dx} \right)^2 - \frac{dg_d(x)}{dx}\frac{d^2 g_d(x)}{d^2 x} \right)}{\sqrt{1 + \left(\frac{dg_d(x)}{dx} \right)^2 + \left(\frac{dh_d(x)}{dx} \right)^2}\sqrt{1 + \left(\frac{dg_d(x)}{dx} \right)^2}} \tag{22}$$

$$a_{zi} = \sqrt{1 + \left(\frac{dg_d(x)}{dx} \right)^2 + \left(\frac{dh_d(x)}{dx} \right)^2}\frac{\dot{f}_d(t)\frac{d^2 g_d(x)}{d^2 x}}{1 + \left(\frac{dg_d(x)}{dx} \right)^2} \tag{23}$$

By applying Equations (21)–(23) to Equation (2), we obtained:

$$\left| \frac{\dot{f}_d^2(t)\left(\frac{d^2 g_d(x)}{d^2 x} + \frac{d^2 h_d(x)}{d^2 x} \right) + \ddot{f}_d(t)\left(\frac{dg_d(x)}{dx} + \frac{dh_d(x)}{dx} \right)}{\sqrt{1 + \left(\frac{dg_d(x)}{dx} \right)^2 + \left(\frac{dh_d(x)}{dx} \right)^2}} \right| \le a_{x\max} \tag{24}$$

$$\left| -\dot{f}_d(t)\frac{\frac{dh_d(x)}{dx}\left(1 + \left(\frac{dg_d(x)}{dx} \right)^2 - \frac{dg_d(x)}{dx}\frac{d^2 g_d(x)}{d^2 x} \right)}{\sqrt{1 + \left(\frac{dg_d(x)}{dx} \right)^2 + \left(\frac{dh_d(x)}{dx} \right)^2}\sqrt{1 + \left(\frac{dg_d(x)}{dx} \right)^2}} \right| \le a_{y\max} \tag{25}$$

$$\left| \sqrt{1 + \left(\frac{dg_d(x)}{dx} \right)^2 + \left(\frac{dh_d(x)}{dx} \right)^2}\frac{\dot{f}_d(t)\frac{d^2 g_d(x)}{d^2 x}}{1 + \left(\frac{dg_d(x)}{dx} \right)^2} \right| \le a_{z\max} \tag{26}$$

Considering Equations (19) and (20), it was obtained that:

$$\left| \frac{\dot{f}_d^2(t)(\lambda_2 + \mu_2) + \ddot{f}_d(t)(\lambda_1 + \mu_1)}{\sqrt{1 + \lambda_1^2 + \mu_1^2}} \right| \le a_{x\max} \tag{27}$$

$$\left| \dot{f}_d(t) \frac{\mu_1 \left(1 + \lambda_1^2 - \lambda_1 \lambda_2\right)}{\sqrt{1 + \lambda_1^2 + \mu_1^2} \sqrt{1 + \lambda_1^2}} \right| \le a_{y\max} \tag{28}$$

$$\left| \sqrt{1 + \lambda_1^2 + \mu_1^2} \frac{\lambda_2 \dot{f}_d(t)}{1 + \lambda_1^2} \right| \le a_{z\max} \tag{29}$$

From Equations (27)–(29), we obtained:

$$\left| \dot{f}_d(t) \right| \le \lambda_3,$$
$$\lambda_3 = \min\left(\sqrt{a_{x\max}}, \frac{a_{y\max} \sqrt{1 + \lambda_1^2 + \mu_1^2} \sqrt{1 + \lambda_1^2}}{1 + \lambda_1^2 - \lambda_1 \lambda_2}, \frac{a_{z\max}\left(1 + \lambda_1^2\right)}{\lambda_2 \sqrt{1 + \lambda_1^2 + \mu_1^2}} \right) \tag{30}$$

$$\left| \ddot{f}_d(t) \right| \le \frac{a_{x\max} \sqrt{1 + \lambda_1^2 + \mu_1^2}}{\lambda_1 + \mu_1} \tag{31}$$

It can be derived from the above equation that when the system input was bounded, the boundedness of the trajectory could be guaranteed. The design of the outer loop controller is discussed below. From Equation (3), the system error tracking equation can be obtained as:

$$\dot{e}_i = \begin{bmatrix} \dot{x}_i - \dot{x}_l \\ \dot{y}_i - \dot{y}_l \\ \dot{z}_i - \dot{z}_l \end{bmatrix} = \begin{bmatrix} v_i \cos \gamma_i \cos \chi_i - v_{xl} \\ v_i \cos \gamma_i \sin \chi_i - v_{yl} \\ -v_i \sin \gamma_i - v_{zl} \end{bmatrix} \tag{32}$$

The outer-loop virtual input can be taken as:

$$\boldsymbol{u}_i = \begin{bmatrix} u_1 \\ u_2 \\ u_3 \end{bmatrix} = \begin{bmatrix} v_i \cos \gamma_i \cos \chi_i \\ v_i \cos \gamma_i \sin \chi_i \\ -v_i \sin \gamma_i \end{bmatrix} = \begin{bmatrix} v_{xl} - a_1 \tanh(\rho_1 e_x) \\ v_{yl} - a_2 \tanh(\rho_2 e_y) \\ v_{zl} - a_3 \tanh(\rho_3 e_z) \end{bmatrix} \tag{33}$$

To achieve the inner loop control when the input is $\boldsymbol{u}_i$, the ideal tracking state of the inner loop can be calculated according to Equation (33) as:

$$\begin{aligned} v_d &= -\frac{u_3}{\sin \gamma_d} \\ \chi_d &= \arctan\left(\frac{u_2}{u_1} \right) \\ \gamma_d &= -\arctan\left(\frac{u_3}{\sqrt{u_1^2 + u_1^2}} \right) \end{aligned} \tag{34}$$

Take the inner-loop sliding mode functions as:

$$\begin{aligned} s_v &= v_i - v_d \\ s_\chi &= \chi_i - \chi_d \\ s_\gamma &= \gamma_i - \gamma_d \end{aligned} \tag{35}$$

The system input can be taken as:

$$a_{xi} = \dot{v}_d - k_1 s_v - \tau_1 \mathrm{sign} s_v - b_1 \tanh \rho_4 s_v \tag{36}$$

$$a_{yi} = -v_d \left(\dot{\gamma}_d - k_2 s_\gamma - \tau_2 \mathrm{sign} s_\gamma - b_2 \tanh \rho_5 s_\gamma \right) \tag{37}$$

$$a_{zi} = v_d \left(\dot{\chi}_d - k_3 s_\chi - \tau_3 \mathrm{sign} s_\chi - b_3 \tanh \rho_6 s_\chi \right) \tag{38}$$

when the system input is (36)–(38), and the system can ensure global stability (Stability proofs are made in the next section).

3.2. System Stability Proof

With the input of Equation (33) for the outer loop system, the tracking error system (32) can become:

$$\dot{e}_i = \begin{bmatrix} \dot{x}_i - \dot{x}_l \\ \dot{y}_i - \dot{y}_l \\ \dot{z}_i - \dot{z}_l \end{bmatrix} = \begin{bmatrix} -a_1 \tanh(\rho_1 e_x) \\ -a_2 \tanh(\rho_2 e_y) \\ -a_3 \tanh(\rho_3 e_z) \end{bmatrix} \tag{39}$$

To prove the stability of the outer-loop system, Theorem 1 is given.

Theorem 1. *When the system has a tame solution, as shown in equation:*

$$\dot{\eta} = -\alpha \tanh(k\eta) \tag{40}$$

for any constant $\alpha.\eta$ satisfying $\alpha.\eta > 0$, the system converges to 0 in any initial state $\eta(0)$.

The proof procedure is shown in [38] and is not repeated here. For the inner-loop system, the Lyapunov function of the inner-loop tracking error system can be taken as:

$$V_1 = \frac{1}{2}s_v^2 + \frac{1}{2}s_\chi^2 + \frac{1}{2}s_\gamma^2 \tag{41}$$

Taking the derivative of Equation (41) and substituting it into Equations (1) and (35), we obtained:

$$\begin{aligned} \dot{V}_1 &= s_v \dot{s}_v + s_\chi \dot{s}_\chi + s_\gamma \dot{s}_\gamma \\ &= s_v(\dot{v}_i - \dot{v}_d) + s_\chi(\dot{\chi}_i - \dot{\chi}_d) + s_\gamma(\dot{\gamma}_i - \dot{\gamma}_d) \\ &= s_v(a_{xi} - \dot{v}_d) + s_\chi\left(\frac{a_{zi}}{v_d} - \dot{\chi}_d\right) + s_\gamma\left(-\frac{a_{yi}}{v_d} - \dot{\gamma}_d\right) \end{aligned} \tag{42}$$

By substituting into Equations (36)–(38), Equation (42) was simplified to obtain:

$$\begin{aligned} \dot{V}_1 &= s_v(a_{xi} - \dot{v}_d) + s_\chi\left(\frac{a_{zi}}{v_d} - \dot{\chi}_d\right) + s_\gamma\left(-\frac{a_{yi}}{v_d} - \dot{\gamma}_d\right) \\ &= -\left(k_1 s_v^2 + k_2 s_\chi^2 + k_3 s_\gamma^2\right) - \left(\tau_1 s_v \text{sign}s_v + \tau_2 s_\chi \text{sign}s_\chi + \tau_3 s_\gamma \text{sign}s_\gamma\right) \\ &\quad -\left(b_1 s_v \tanh\rho_4 s_v + b_2 s_\chi \tanh\rho_5 s_\chi + b_3 s_\gamma \tanh\rho_6 s_\gamma\right) \\ &< -\left(b_1 s_v \tanh\rho_4 s_v + b_2 s_\chi \tanh\rho_5 s_\chi + b_3 s_\gamma \tanh\rho_6 s_\gamma\right) \end{aligned} \tag{43}$$

Based on Equation (43) and Theorem 1, it was obtained that the inner loop of the system was convergent under the action of the input, and when the parameter values were appropriate, the inner loop converged faster than the outer loop, and the inner and outer loops converged equally when and only when the error was zero. The global stability of the system is analyzed below. Assuming that there exists a pitch angle as well as a deflection angle to satisfy the follower for the leader, the position state part of Equation (1) can be written as:

$$\begin{cases} \dot{x}_i = v_d \cos\gamma_d \cos\chi_d + \cos\gamma_d \cos\chi_d(v_i - v_d) + v_i \cos\gamma_i(\cos\chi_i - \cos\chi_d) + v_i \cos\chi_d(\cos\gamma_i - \cos\gamma_d) \\ \dot{y}_i = v_d \cos\gamma_d \sin\chi_d + \cos\gamma_d \sin\chi_d(v_i - v_d) + v_i \cos\gamma_i(\sin\chi_i - \sin\chi_d) + v_i \sin\chi_d(\cos\gamma_i - \cos\gamma_d) \\ \dot{z}_i = -v_d \sin\gamma_d - \sin\gamma_d(v_i - v_d) - v_i(\sin\gamma_i - \sin\gamma_d) \end{cases} \tag{44}$$

From Equation (44), the state tracking system produces corresponding deviations when there are errors in χ_i, χ_d as well as γ_i, γ_d. Considering that the system inputs (36) to (38) were bounded, the system state quantity v_i, χ_i, γ_i satisfies the global Lipschitz condition. Substituting the outer-loop reference control and inputting them into Equation (44) yielded:

$$\begin{cases} \dot{e}_x = -a_1\tanh(\rho_1 e_x) + \cos\gamma_d\cos\chi_d(v_i - v_d) + v_i\cos\gamma_i(\cos\chi_i - \cos\chi_d) + v_i\cos\chi_d(\cos\gamma_i - \cos\gamma_d) \\ \dot{e}_y = -a_2\tanh(\rho_2 e_y) + \cos\gamma_d\sin\chi_d(v_i - v_d) + v_i\cos\gamma_i(\sin\chi_i - \sin\chi_d) + v_i\sin\chi_d(\cos\gamma_i - \cos\gamma_d) \\ \dot{e}_z = -a_3\tanh(\rho_3 e_z) - \sin\gamma_d(v_i - v_d) - v_i(\sin\gamma_i - \sin\gamma_d) \end{cases} \quad (45)$$

The following is an example of analyzing the stability of the system with e_x. the system Lyapunov function can be taken as:

$$V = 3a_1\ln(\cosh\rho_1 e_x) + \frac{1}{2}\rho_1 e_x^2 \quad (46)$$

where $\alpha, \rho_1 > 0$. Taking the derivative of Equation (46) leads to,

$$\dot{V} = 3a_1\rho_1\dot{e}_x\tanh\rho_1 e_x + \rho_1 e_x\dot{e}_x \quad (47)$$

Let $m_1 = a_1\tanh(\rho_1 e_x)$, $m_2 = \cos\gamma_d\cos\chi_d(v_i - v_d)$, $m_3 = v_i\cos\gamma_i(\cos\chi_i - \cos\chi_d)$, $m_4 = v_i\cos\chi_d(\cos\gamma_i - \cos\gamma_d)$, then $\dot{e}_x$ can be expressed as: $\dot{e}_x = -m_1 + m_2 + m_3 + m_4$, and, when substituted into Equation (47), gives:

$$\begin{aligned} \dot{V}_{e_x} &= 3\rho_1 m_1(-m_1 + m_2 + m_3 + m_4) + \rho_1 e_x(-m_1 + m_2 + m_3 + m_4) \\ &= -\rho_1\left[m_1^2 - 3m_1 m_2 + \left(\tfrac{3}{2}m_2\right)^2\right] - \rho_1\left[m_1^2 - 3m_1 m_2 + \left(\tfrac{3}{2}m_2\right)^2\right] - \rho_1\left[m_1^2 - 3m_1 m_2 + \left(\tfrac{3}{2}m_2\right)^2\right] \\ &\quad -\rho_1 e_x m_1 + \tfrac{9}{4}\rho_1 m_2(m_2 + e_x) + \tfrac{9}{4}\rho_1 m_3(m_3 + e_x) + \tfrac{9}{4}\rho_1 m_3(m_3 + e_x) \end{aligned}$$

Additionally, because of $a_1\tanh(\rho_1 e_x) > 0$, therefore:

$$\begin{aligned} \dot{V}_{e_x} &< -\rho_1\left[m_1^2 - 3m_1 m_2 + \left(\tfrac{3}{2}m_2\right)^2\right] - \rho_1\left[m_1^2 - 3m_1 m_2 + \left(\tfrac{3}{2}m_2\right)^2\right] - \rho_1\left[m_1^2 - 3m_1 m_2 + \left(\tfrac{3}{2}m_2\right)^2\right] \\ &\quad +\tfrac{9}{4}\rho_1 m_2(m_2 + e_x) + \tfrac{9}{4}\rho_1 m_3(m_3 + e_x) + \tfrac{9}{4}\rho_1 m_3(m_3 + e_x) \\ &< -\rho_1\left[\left(m_1 - \tfrac{3}{2}m_2\right)^2 + \left(m_1 - \tfrac{3}{2}m_3\right)^2 + \left(m_1 - \tfrac{3}{2}m_4\right)^2\right] \\ &\quad +\tfrac{9}{4}\rho_1 m_2(m_2 + e_x) + \tfrac{9}{4}\rho_1 m_3(m_3 + e_x) + \tfrac{9}{4}\rho_1 m_3(m_3 + e_x) \end{aligned} \quad (48)$$

Additionally, the following can be considered:

$$|\cos\chi_i - \cos\chi_d| = \left|2\sin\frac{\chi_i + \chi_d}{2}\sin\frac{\chi_i - \chi_d}{2}\right| \le 2\left|\sin\frac{\chi_i - \chi_d}{2}\right| \le |\chi_i - \chi_d| \quad (49)$$

The same reasoning leads to:

$$|\cos\gamma_i - \cos\gamma_d| \le |\gamma_i - \gamma_d| \quad (50)$$

From Equation (43), v_i, γ_i, χ_i is exponentially convergent. For $\forall\varepsilon > 0$, $\exists t_{v_i} > 0$, when $t > t_{v_i}$, $|v_i - v_d| < \varepsilon$; similarly, this applies when $t > t_{\chi_i}$, $|\chi_i - \chi_d| < \varepsilon$ and when $t > t_{\gamma_i}$, $|\gamma_i - \gamma_d| < \varepsilon$. So, there exists a finite time t_{e_x}, when $t_{e_x} > \max\{t_{v_i}, t_{\chi_i}, t_{\gamma_i}\}$, $\dot{V}_{e_x} < 0$ and when $t \to \infty$, $m_i \to 0$, $(i = 2, 3, 4)$. So when $t \to \infty$, $e_x \to 0$, Similarly, it can be proved that when $t \to \infty$, $e_y \to 0$, $e_z \to 0$, and the global stability of the system is proved.

3.3. Delayed System Stability Proof

When the navigator exists within the field of view of the follower UAV, the system can achieve tracking in a time-delay-free state. However, when the navigator is not present in the field of view of the follower UAV, there is a time delay in the state transfer, and Theorem II is given below and demonstrates that the delayed system can achieve convergence.

Theorem 2. *When the time delay of system* $\lim_{t\to\infty} x_{l-4} = x_r$ *is h, satisfying* $h > 0, h \in \left(0, \overline{h}\right]$, $\overline{h}$ *appears as the upper limit of delay, then when:*

$$
\Gamma(h) =
\begin{bmatrix}
Q_1 & 0 & 0 & P_1 A_{12r} \\
0 & -Q_1 & 0 & 0 \\
0 & 0 & -hZ_1 & 0 \\
A_{12r}^T P_1 & 0 & 0 & A_{12r}^T hZ_1 A_{12r} + P_2 A_{22r} + A_{22r}^T P_2 + Q_2 + A_{22r}^T hZ_2 A_{22r} \\
A_{12d}^T P & 0 & 0 & A_{12d}^T hZ_1 A_{12r} + A_{22d}^T P_2 + A_{22d}^T hZ_2 A_{22r} \\
0 & 0 & 0 & 0 \\
0 & 0 & 0 & B_{2r}^T P_2 + B_{2r}^T hZ_2 A_{22r} \\
0 & 0 & 0 & B_{2d}^T P_2 + B_{2d}^T hZ_2 A_{22r}
\end{bmatrix}
$$

$$
\begin{bmatrix}
P_1 A_{12d} & 0 & 0 & 0 \\
0 & 0 & 0 & 0 \\
0 & 0 & 0 & 0 \\
A_{12r}^T hZ_1 A_{12d} + P_2 A_{22d} + A_{22r}^T hZ_2 A_{22d} & 0 & P_2 B_{2r} + A_{22r}^T hZ_2 B_{2r} & P_2 B_{2d} + A_{22r}^T hZ_2 B_{2d} \\
A_{12d}^T hZ_1 A_{12d} - Q_2 + A_{22d}^T hZ_2 A_{22d} & 0 & A_{22d}^T hZ_2 B_{2r} & A_{22d}^T hZ_2 B_{2d} \\
0 & -hZ_2 & 0 & 0 \\
B_{2r}^T hZ_2 A_{22d} & 0 & R + B_{2r}^T hZ_2 B_{2r} & B_{2r}^T hZ_2 B_{2d} \\
B_{2d}^T hZ_2 A_{22d} & 0 & B_{2d}^T hZ_2 B_{2r} & B_{2d}^T hZ_2 B_{2d} - R
\end{bmatrix} < 0
$$

this indicates delayed system stability. Among others, $P_1, Z_1, P_2, Q, R, Z_2 > 0$.

Proof of Theorem 2. First, linearizing the error state Equation (32) results in:

$$
\dot{e}_i = A e_i + B u_i \tag{51}
$$

where:

$$
\begin{aligned}
A &= \begin{bmatrix} A_{11} & A_{12} \\ A_{13} & A_{14} \end{bmatrix} \\
&= \begin{bmatrix}
0 & 0 & 0 & \cos\gamma_r \cos\chi_r & -v_r \cos\gamma_r \sin\chi_r & -v_r \sin\gamma_r \cos\chi_r \\
0 & 0 & 0 & \cos\gamma_r \sin\chi_r & v_r \cos\gamma_r \cos\chi_r & -v_r \sin\gamma_r \sin\chi_r \\
0 & 0 & 0 & \sin\gamma_r & 0 & v_r \cos\gamma_r \\
0 & 0 & 0 & 0 & 0 & 0 \\
0 & 0 & 0 & -1/v_r^2 & 0 & 0 \\
0 & 0 & 0 & -1/v_r^2 & 0 & 0
\end{bmatrix}, \quad
B = \begin{bmatrix} B_{11} \\ B_{21} \end{bmatrix} = \begin{bmatrix}
0 & 0 & 0 \\
0 & 0 & 0 \\
0 & 0 & 0 \\
1 & 0 & 0 \\
0 & 1/v_r & 0 \\
0 & 0 & -1/v_r
\end{bmatrix}
\end{aligned}
$$

namely,

$$
\begin{aligned}
\dot{e}_1(t) &= A_{12r} e_2(t) + A_{12d} e_2(t - h) \\
\dot{e}_2(t) &= A_{22r} e_2(t) + A_{22d} e_2(t - h) + B_{2r} u(t) + B_{2d} u(t - h)
\end{aligned} \tag{52}
$$

where A_{12r}, A_{22r}, B_{2r} is the ideal state error matrix and A_{12d}, A_{22d}, B_{2d} is the error between the ideal state matrix and the actual matrix. The Lyapunov–Krasovskii generalized function can be taken as follows.

$$
\begin{aligned}
V_3(e_2, t) &= e_1^T(t)P_1 e_1(t) \\
V_4(e_2, t) &= \int_{t-h}^{t} e_1^T(\alpha)Q_1 e_1(\alpha) d\alpha \\
V_5(e_2, t) &= \int_{-h}^{0} \int_{t-h}^{t} \dot{e}_1^T(t)Z_1 \dot{e}_1(t) d\alpha d\beta \\
V_6(e_2, t) &= e_2^T(t)P_2 e_2(t) \\
V_7(e_2, t) &= \int_{t-h}^{t} e_2^T(\alpha)Q_2 e_2(\alpha) d\alpha \\
V_8(u_2, t) &= \int_{t-h}^{t} u_2^T(t)R u_2(t) d\alpha \\
V_9(e_2, t) &= \int_{-h}^{0} \int_{t-h}^{t} \dot{e}_2^T(t)Z_2 \dot{e}_2(t) d\alpha d\beta
\end{aligned}
\tag{53}
$$

where $P_1, Z_1, P_2, Q, R, Z_2 > 0$, and it is clear that the above equation satisfies this.

$$
V(e, t) = \sum_{i=3}^{8} V_i(e, t) > 0
\tag{54}
$$

From the system (52), the derivative of Equation (53) can be obtained as:

$$
\begin{aligned}
\dot{V}_3(e_1, t) &= 2e_1^T(t)P_1 \dot{e}_1(t) \\
&= 2e_1^T(t)P_1 A_{12r} e_2(t) + 2e_1^T(t)P_1 A_{12d} e_2(t-h) + 2e_1^T(t)P_1 w_1(t) \\
&= \frac{1}{h}\int_{t-h}^{t} \left[2e_1^T(t)P_1 A_{12r} e_2(t) + 2e_1^T(t)P_1 A_{12d} e_2(t-h) + 2e_1^T(t)P_1 w_1(t) \right] d\alpha
\end{aligned}
\tag{55}
$$

$$
\dot{V}_4(e_1, t) = \frac{1}{h}\int_{t-h}^{t} \left[e_1^T(t)Q_1 e_1(t) - e_1^T(t-h)Q_1 e_1(t-h) \right] d\alpha
\tag{56}
$$

$$
\begin{aligned}
\dot{V}_5(e_1, t) &= \int_{-h}^{0} \int_{t-h}^{t} \dot{e}_1^T(t)Z_1 \dot{e}_1(t) d\alpha d\beta \\
&= \int_{t-h}^{t} \left[\dot{e}_1^T(t)Z_1 \dot{e}_1(t) - \dot{e}_1^T(t+\beta)Z_1 \dot{e}_1(t+\beta) \right] d\beta \\
&\overset{t+\beta=\alpha}{=} \int_{t-h}^{t} \left[\dot{e}_1^T(t)Z_1 \dot{e}_1(t) - \dot{e}_1^T(\alpha)Z_1 \dot{e}_1(\alpha) \right] d\alpha \\
&= \frac{1}{h}\int_{t-h}^{t} h \begin{bmatrix} (A_{12r}e_2(t) + A_{12d}e_2(t-h) + w_1(t))^T Z_1 (A_{12r}e_2(t) + A_{12d}e_2(t-h) + w_1(t)) \\ -\dot{e}_1^T(\alpha)Z_1 \dot{e}_1(\alpha) \end{bmatrix} d\alpha
\end{aligned}
\tag{57}
$$

$$
\begin{aligned}
\dot{V}_6(e_2, t) &= 2e_2^T(t)P_2 \dot{e}_2(t) \\
&= 2e_2^T(t)P_2 A_{22r} e_2(t) + 2e_2^T(t)P_2 A_{22d} e_2(t-h) \\
&\quad + 2e_2^T(t)P_2 B_{2r} u(t) + 2e_2^T(t)P_2 B_{2d} u(t-h) \\
&= \frac{1}{h}\int_{t-h}^{t} \begin{bmatrix} 2e_2^T(t)P_2 A_{22r} e_2(t) + 2e_2^T(t)P_2 A_{22d} e_2(t-h) \\ +2e_2^T(t)P_2 B_{2r} u(t) + 2e_2^T(t)P_2 B_{2d} u(t-h) \end{bmatrix} d\alpha
\end{aligned}
\tag{58}
$$

$$
\dot{V}_7(e_2, t) = \frac{1}{h}\int_{t-h}^{t} \left[e_2^T(t)Q_2 e_2(t) - e_2^T(t-h)Q_2 e_2(t-h) \right] d\alpha
\tag{59}
$$

$$
\dot{V}_8(u_2, t) = \frac{1}{h}\int_{t-h}^{t} \left[u_2^T(t)R u_2(t) - u_2^T(t-h)R u_2(t-h) \right] d\alpha
\tag{60}
$$

$$
\begin{aligned}
\dot{V}_9(\boldsymbol{e}_2, t) &= \int_{-h}^{0} \int_{t-h}^{t} \dot{\boldsymbol{e}}_2^T(t) \boldsymbol{Z}_2 \dot{\boldsymbol{e}}_2(t) d\alpha d\beta \\
&= \int_{t-h}^{t} \left[\dot{\boldsymbol{e}}_2^T(t) \boldsymbol{Z}_2 \dot{\boldsymbol{e}}_2(t) - \dot{\boldsymbol{e}}_2^T(t+\beta) \boldsymbol{Z}_2 \dot{\boldsymbol{e}}_2(t+\beta) \right] d\beta \\
&\overset{t+\beta=\alpha}{=} \int_{t-h}^{t} \left[\dot{\boldsymbol{e}}_2^T(t) \boldsymbol{Z}_2 \dot{\boldsymbol{e}}_2(t) - \dot{\boldsymbol{e}}_2^T(\alpha) \boldsymbol{Z}_2 \dot{\boldsymbol{e}}_2(\alpha) \right] d\alpha \\
&= \frac{1}{h} \int_{t-h}^{t} h \begin{bmatrix} (\boldsymbol{A}_{22r}\boldsymbol{e}_2(t) + \boldsymbol{A}_{22d}\boldsymbol{e}_2(t-h) + \boldsymbol{B}_{2r}\boldsymbol{u}(t) + \boldsymbol{B}_{2d}\boldsymbol{u}(t-h))^T \\ h\boldsymbol{Z}_2(\boldsymbol{A}_{22r}\boldsymbol{e}_2(t) + \boldsymbol{A}_{22d}\boldsymbol{e}_2(t-h) + \boldsymbol{B}_{2r}\boldsymbol{u}(t) + \boldsymbol{B}_{2d}\boldsymbol{u}(t-h)) \\ -\dot{\boldsymbol{e}}_2^T(\alpha) \boldsymbol{Z}_2 \dot{\boldsymbol{e}}_2(\alpha) \end{bmatrix} d\alpha
\end{aligned}
\tag{61}
$$

From Equations (55)–(61), it can be obtained that:

$$
\dot{V}(\boldsymbol{e}, t) = \frac{1}{h} \int_{t-h}^{t} \left[\Xi^T(t, \alpha) \Gamma(h) \Xi(t, \alpha) \right] d\alpha
\tag{62}
$$

where:

$$
\Xi(t, \alpha) = \begin{bmatrix} \boldsymbol{e}_1(t) & \boldsymbol{e}_1(t-h) & \dot{\boldsymbol{e}}_1(\alpha) & \boldsymbol{e}_2(t) & \boldsymbol{e}_2(t-h) & \dot{\boldsymbol{e}}_2(\alpha) & \boldsymbol{u}(t) & \boldsymbol{u}(t-h) \end{bmatrix},
$$

So, when $\Gamma(h) < 0$, $\dot{V}(\boldsymbol{e}, t) < 0$, theorem II can be proved. $\square$

4. Simulation and Test Results

In order to verify the algorithm proposed in this paper, the control algorithm proposed was simulated with MATLAB, as outlined in this section. We assumed that the UAVs used for simulation carried onboard sensors that were capable of measuring the relative distance, relative pitch, and relative yaw angles. The simulation parameters were set as shown in Table 1. The initial states of the drones are shown in Table 2.

Table 1. Simulation parameters table.

Parameter Name	Symbols	Numerical Value
Sampling interval	T_k	0.01
Sampling time	T	30
Number of drones	N_v	4
Intermachine delay	h	0.004

Table 2. UAV initial parameter table.

UAV Number	Initial Location	$v(m/s)$	Yaw Angle
1	$[2, -2, 0]^T$	0	$\frac{\pi}{3}$
2	$[-2, 3, 0]^T$	0	$\frac{\pi}{3}$
3	$[2, -1, 0]^T$	0	$\frac{\pi}{3}$
4	$[-2, -1, 0]^T$	0	$\frac{\pi}{3}$

4.1. Case 1

In case 1, we first simulated the case of four UAVs in formation in a simple curve environment. The simulation results are shown in Figures 4–9. We set the desired trajectory as:

$$
\begin{bmatrix} x_d & y_d & z_d \end{bmatrix}^T = \begin{bmatrix} t & \sin(0.5 \times x_d) + 0.5 \times x_d + 0.5 & x_d \end{bmatrix}^T
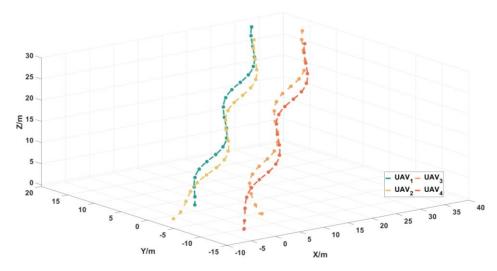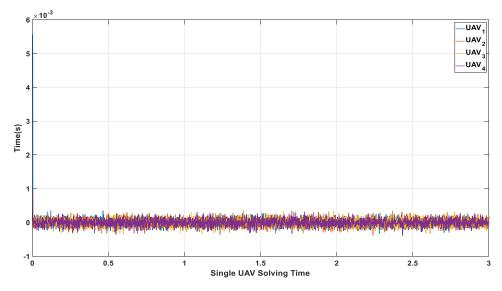$$

Figure 4. UAV trajectory.
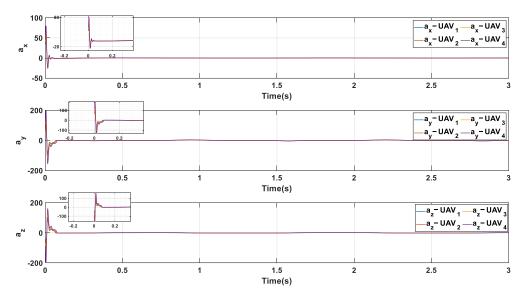

Figure 5. Single UAV solving time.
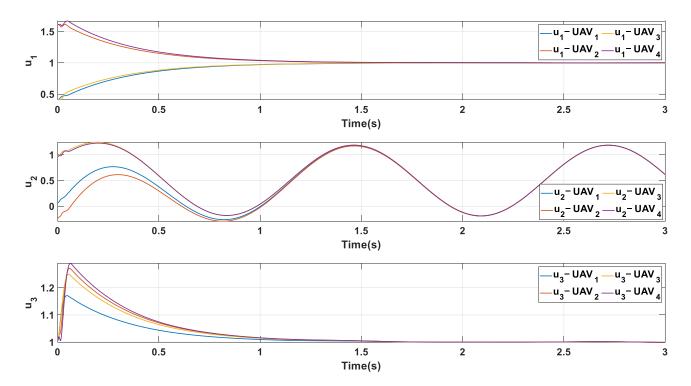

Figure 6. Actual UAV input.

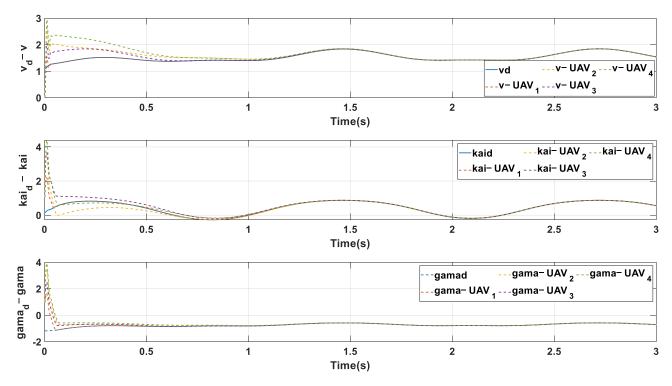**Figure 7.** UAV virtual input.

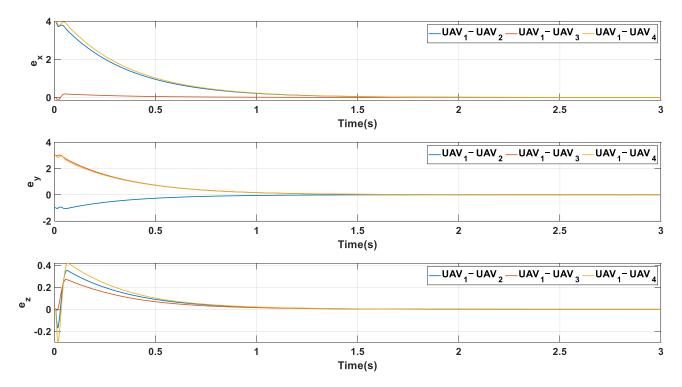**Figure 8.** Attitude error.

Figure 9. Position error.

As can be seen in Figure 4, the UAV is able to achieve the expected formation control and maintain the stability of the formation until the end of the simulation, verifying the effectiveness of the algorithm in simple curved paths. Additionally, when the leader is not in the follower's field of view, and there is a certain delay in state transfer, No. 4 is able to follow the leader effectively. In Figure 5, at the first sampling moment, the solution time of the UAV controller of No. 1 was significantly higher than that of the other UAVs, but it was less than 0.01 s, verifying that the controller could complete the solution within the sampling time to avoid the errors caused by an untimely solution. Figure 6 shows the acceleration input of the UAV during the actual motion, and it can be seen that the algorithm of this controller avoided the jitter of the input. Figure 7 gives the virtual input of the system calculated based on the UAV position error, from which it can be seen that the virtual input was able to generate a continuous inner-loop control signal (as shown in Figure 8 for the inner-loop ideal tracking state). Regardless of the UAV state volume (as shown in Figure 8) or the position error (as shown in Figure 9), the following UAV was able to achieve finite time convergence, while the inner loop convergence rate was greater than the outer loop convergence rate, ensuring the convergence of the system.

4.2. Case 2

In case 2, we simulated the formation control and retention problem of four UAVs in a complex path, and the simulation results are shown in Figures 9–13. We set the desired trajectory as:

$$\begin{bmatrix} x_d & y_d & z_d \end{bmatrix}^T = \begin{bmatrix} t & 5 \times \sin(0.5 \times x_d) & 5 \times \cos(0.5 \times x_d) + 0.5 \times x_d \end{bmatrix}^T$$
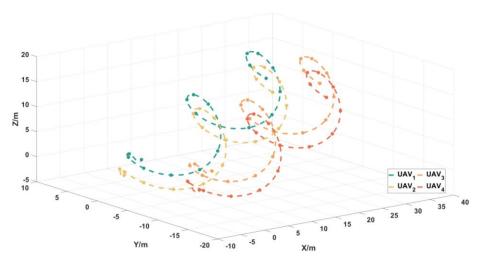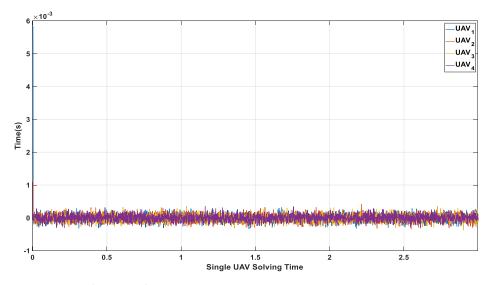
Figure 10. UAV trajectory.

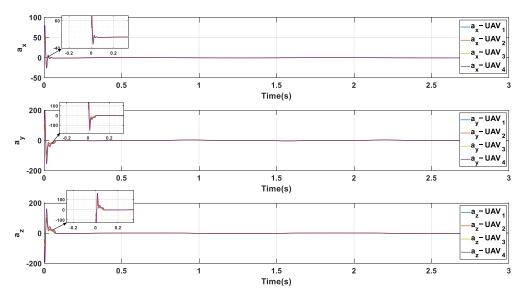**Figure 11.** Single UAV solving time.
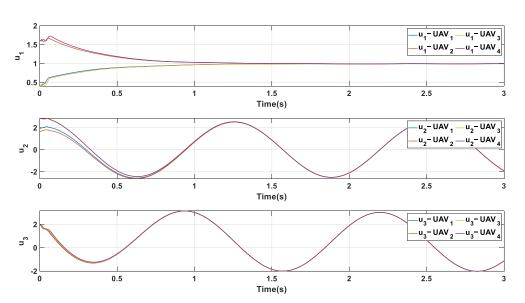

Figure 12. Actual UAV input.

Figure 13. UAV virtual input.

In Figure 10 of case 2, it can be seen that the four UAVs were still able to achieve the formation and maintenance of the formation under complex path conditions, but the tracking effect was not particularly good in the initial phase when the UAVs started tracking, and further improvement is needed in the next step of work. From Figure 11, it can be seen that the No. 1 UAV and No. 2 UAV had a long controller calculation time in the first sampling moment, and the controller solution time within the cluster was less than 0.01 s. In Figure 12, it can be seen that the inputs of the four UAVs were still able to achieve formation control and acceleration convergence in a short time in a complex environment. Additionally, as can be seen in Figure 13, when the path was continuous, the generated virtual inputs were also continuous and could provide continuous desired signals to the inner loop control. In Figures 14 and 15, it can be seen that the state, as well as the position error of the UAV, can achieve fast convergence under the action of the algorithm, and the inner loop converged faster than the outer loop converges, which ensured the formation and maintenance of the formation.
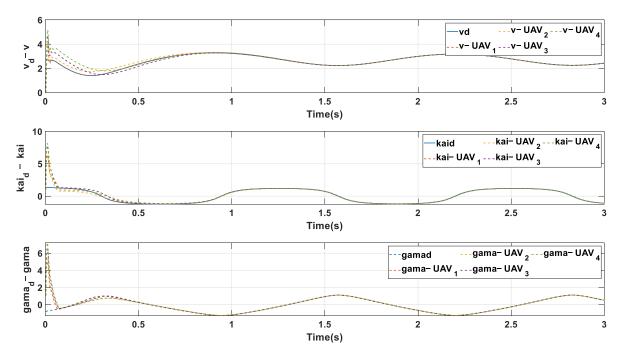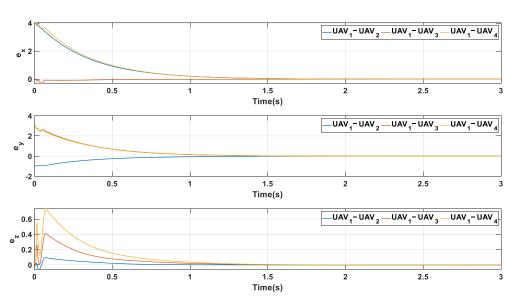

Figure 14. Attitude error.

Figure 15. Position error.

4.3. Case 3

To further verify the effectiveness of the algorithm for the formation control of large-scale clusters, the formation control of eight UAVs was simulated in a complex environment with the initial states of the UAVs shown in Table 3, and the simulation results are shown in Figure 14–18. In case 3, we set the desired trajectory as:

$$\begin{bmatrix} x_d & y_d & z_d \end{bmatrix}^T = \begin{bmatrix} t & 5 \times \sin(0.5 \times x_d) & 5 \times \cos(0.5 \times x_d) + 0.5 \times x_d \end{bmatrix}^T$$

Table 3. UAV initial parameter table.

UAV Number	Initial Location	$v(m/s)$	Yaw Angle
1	$[2, -2, 0]^T$	0	$\frac{\pi}{3}$
2	$[-2, 3, 0]^T$	0	$\frac{\pi}{3}$
3	$[2, -1, 0]^T$	0	$\frac{\pi}{3}$
4	$[-2, -1, 0]^T$	0	$\frac{\pi}{3}$
5	$[-2, 2, 0]^T$	0	$\frac{\pi}{3}$
6	$[2, -3, 0]^T$	0	$\frac{\pi}{3}$
7	$[-2, 1, 0]^T$	0	$\frac{\pi}{3}$
8	$[-2, -2, 0]^T$	0	$\frac{\pi}{3}$

In Figure 16, it can be seen that the eight UAVs were able to effectively achieve and maintain an ideal formation under the action of the algorithm, but there was also a situation where some of the UAVs were poorly tracked during the initial phase, which required correcting in the next step to ensure that the system could achieve stability from the initial state under various paths. In Figure 17, it is shown that among the cluster of 8 UAVs, there existed 3 UAVs (UAVs No. 1,3,5) whose first solving time is much longer than the other sorties, and all other numbered UAVs were able to satisfy the solving of the controller within one sampling moment. In Figure 18, it can be seen that the acceleration of each UAV experienced large fluctuations in the initial state, and after the system error started to converge, the system input gradually converged, and the amplitude decreased, ensuring the formation control at low acceleration. Figure 19 then shows that the virtual inputs of each UAV gradually converged after stabilization and were able to provide

a stable and continuous tracking signal to the inner loop (as shown in Figure 20). In Figures 20 and 21, the UAV inner-loop state error, as well as the outer-loop position error are given, respectively; from this, it can be seen that the large-scale cluster could achieve the convergence of the state error as well as formation control in the complex path case.
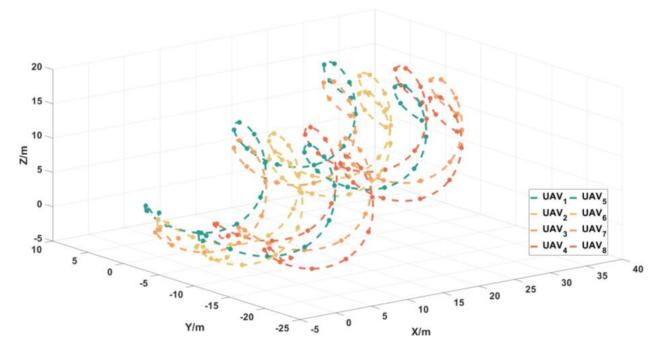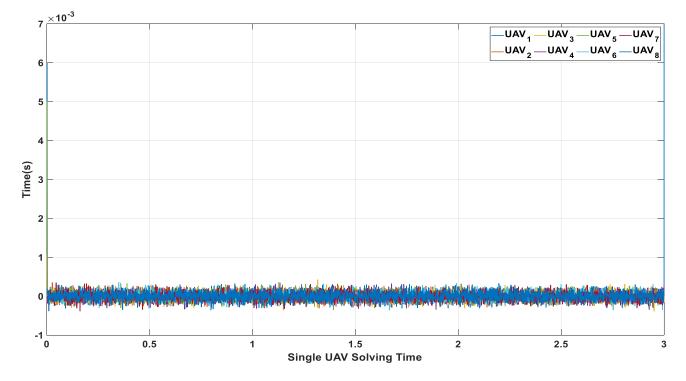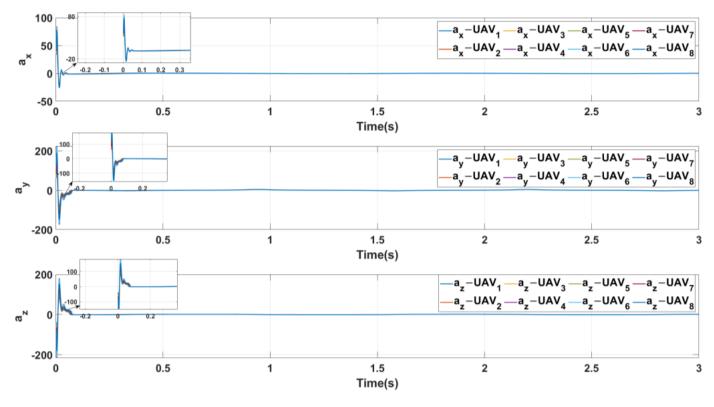

Figure 16. UAV trajectory.

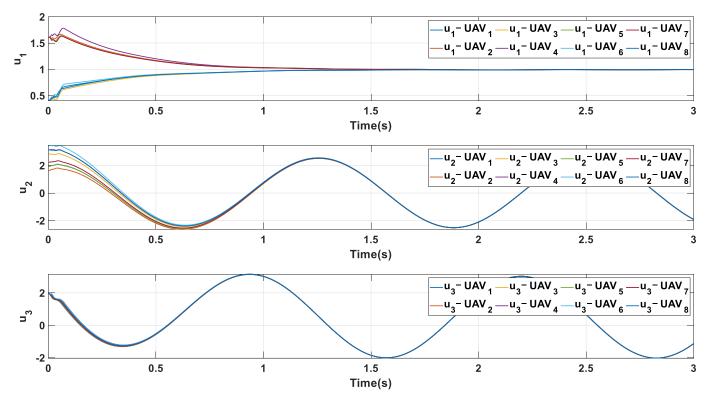

Figure 17. Single UAV solving time.

Figure 18. Actual UAV input.
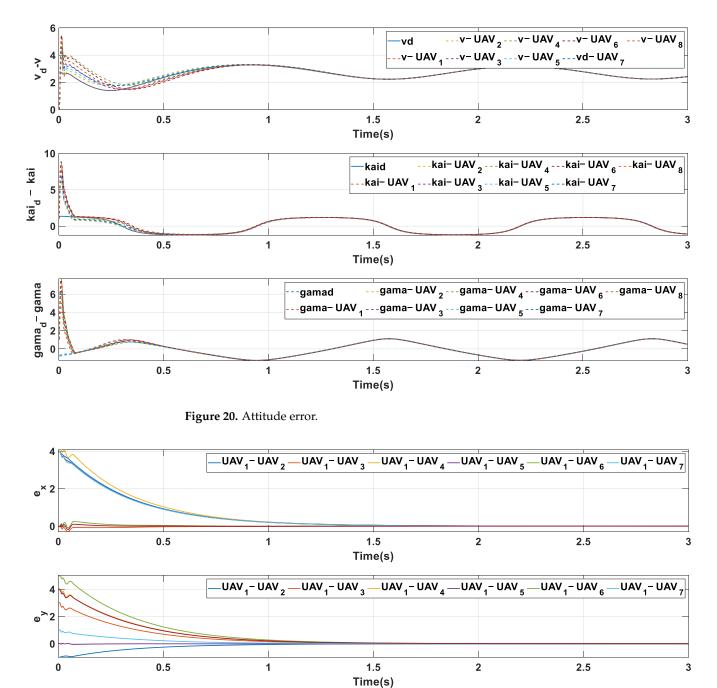

Figure 19. UAV virtual input.

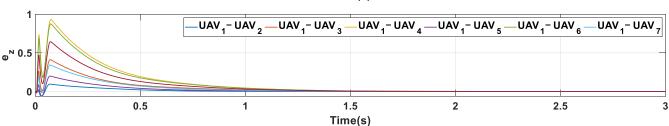**Figure 20.** Attitude error.

Figure 21. Position error.

4.4. Discussion

From the above three numerical simulation examples, it can be seen that:

1. The designed controller can be effectively applied to the formation control of fixed-wing UAVs, even in the presence of measurement errors as well as state transfer time delays in multiple UAV formations.
2. It can be seen from the computation times of the three examples that, since the controller was distributed, it did not increase the solution time of individual UAVs as the number of UAVs increased. However, there was a long initial moment at the beginning of each phase in the time of each numerical simulation, which would be the next step to improve.
3. When there were multiple UAVs in the neighborhood, the selection of the follower UAV for the desired leader UAV became an issue. In the next step of the study, rules need to be developed or the research method updated to ensure the efficiency and accuracy of the follower UAV's selection of the desired leader UAV.

5. Conclusions

In this paper, a global sliding mode control algorithm for the vision-based control of multiple UAV formations was proposed. In the presence of sensor errors, the follower UAV uses extended Kalman filtering to achieve an estimate of the position as well as the state of the leader UAV in the field of view, and the follower UAV uses the estimated position as a reference value for the local outer loop control. After that, the continuous signal of the inner loop control reference is generated using the outer loop virtual control, which is then passed to the inner loop. Later, the inner-loop controller was designed to ensure the tracking of the inner-loop reference signal, and it was mathematically proven that the inner-loop controller converged faster than the outer loop while the stability of the global algorithm was demonstrated. Finally, the stability of the formation in the presence of time delay was given considering the time delay in the transmission of the ideal state of the UAV due to the limited range of action of the UAV sensors. In a future study, this algorithm will be further investigated in its initial state for the tracking of the reference value, the control of a larger number of clusters, and the further improvement of the algorithm in the case of poor initial state tracking.

Author Contributions: Conceptualization, Q.C. and Y.J.; methodology, Q.C.; validation, Q.C., T.W. and B.Q.; formal analysis, Q.C. and T.W.; investigation, Y.W.; resources, Y.W.; data curation, Y.W. and B.Q.; writing—original draft preparation, Q.C. and Y.J.; writing—review and editing, Y.W. and B.Q.; visualization, T.W.; supervision, T.W. and Y.J. All authors have read and agreed to the published version of the manuscript.

Data Availability Statement: The data used in the experiments are available in the paper.

References

1. Alsamhi, S.H.; Shvetsov, A.V.; Kumar, S.; Shvetsova, S.V.; Alhartomi, M.A.; Hawbani, A.; Rajput, N.S.; Srivastava, S.; Saif, A.; Nyangaresi, V.O. UAV Computing-Assisted Search and Rescue Mission Framework for Disaster and Harsh Environment Mitigation. *Drones* **2022**, *6*, 154. [CrossRef]
2. Radmanesh, M.; Kumar, M. Flight formation of UAVs in presence of moving obstacles using fast-dynamic mixed integer linear programming. *Aerosp. Sci. Technol.* **2016**, *50*, 149–160. [CrossRef]
3. Madyastha, V.K.; Caliset, A.J. An adaptive filtering approach to target tracking. In Proceedings of the American Control Conference, Portland, OR, USA, 8–10 June 2005.
4. Alsamhi, S.H.; Shvetsov, A.V.; Kumar, S.; Hassan, J.; Alhartomi, M.A.; Shvetsova, S.V.; Sahal, R.; Hawbani, A. Computing in the Sky: A Survey on Intelligent Ubiquitous Computing for UAV-Assisted 6G Networks and Industry 4.0/5.0. *Drones* **2022**, *7*, 177. [CrossRef]
5. Alsamhi, S.H.; Ma, O.; Ansari, M.S.; Gupta, S.K. Collaboration of Drone and Internet of Public Safety Things in Smart Cities: An Overview of QoS and Network Performance Optimization. *Drones* **2019**, *3*, 13. [CrossRef]
6. Desai, J.P.; Ostrowski, J.P.; Kumar, V. Modeling and control of formations of nonholonomic mobile robots. *IEEE Trans. Robot. Autom.* **2001**, *17*, 905–908. [CrossRef]

7.   Roldão, V.; Cunha, R.; Cabecinhas, D.; Silvestre, C.; Oliveira, P. A leader-following trajectory generator with application to quadrotor formation flight. *Robot. Auton. Syst.* **2014**, *62*, 1597–1609. [CrossRef]
8.   Fierro, R.; Belta, C.; Desai, J.P.; Kumar, V. On controlling aircraft formations. In Proceedings of the 40th IEEE Conference on Decision and Control (Cat. No.01CH37228), Orlando, Fl, USA, 4–7 December 2001; Volume 2, pp. 1065–1070.
9.   Eren, T. Formation shape control based on bearing rigidity. *Int. J. Control.* **2012**, *85*, 1361–1379. [CrossRef]
10. Lewis, M.A.; Tan, K.H. High precision formation control of mobile robots using virtual structures. *Auton. Robots. Auton. Robot.* **1997**, *4*, 387–403. [CrossRef]
11. Sharma, R.; Ghose, D. Collision avoidance between UA V clusters using swarm intelligence techniques. *Int. J. Syst. Sci.* **2009**, *5*, 521–538. [CrossRef]
12. Giulietti, F.; Innocenti, M.; Pollini, L. Formation flight control—A behavioral approach. In Proceedings of the AIAA Guidance, Navigation, and Control Conference and Exhibit, Montreal, QC, Canada, 6–9 August 2001.
13. Park, C.; Tahk, M.; Bang, H. Multiple Aerial Vehicle Formation Using Swarm Intelligence. In Proceedings of the AIAA Guidance, Navigation, and Control Conference and Exhibit, Austin, TX, USA, 11–14 August 2003.
14. Ren, W. Consensus based formation control strategies for multi-vehicle systems. In Proceedings of the 2006 American Control Conference, Minneapolis, MN, USA, 14–16 June 2006.
15. Jadbabaie, A.; Lin, J.; Morse, A.S. Coordination of groups of mobile autonomous agents using nearest neighbor rules. *IEEE Trans. Autom.* **2003**, *6*, 988–1001. [CrossRef]
16. Wang, X.; Yu, Y.; Li, Z. Distributed sliding mode control for leader-follower formation flight of fixed-wing unmanned aerial vehicles subject to velocity constraints. *Int. J. Robust Nonlinear Control* **2021**, *31*, 2110–2125. [CrossRef]
17. Liu, S.; Tan, D.; Liu, G. Robust Leader-follower Formation Control of Mobile Robots Based on a Second Order Kinematics Model. *Acta Autom. Sin.* **2007**, *33*, 947–955. [CrossRef]
18. Zhao, C.; Dai, S.; Zhao, G.; Gao, C.; Liu, S. UAV formation control based on distributed model predictive control. *Control. Decis.* **2021**, *1*, 1–9.
19. Kim, S.; Cho, H.; Jung, D. Evaluation of Cooperative Guidance for Formation Flight of Fixed-wing UAVs using Mesh Network. In Proceedings of the 2020 International Conference on Unmanned Aircraft Systems, Athens, Greece, 1–4 September 2020.
20. Parivallal, A.; Sakthivel, R.; Amsaveni, R.; Alzahrani, F.; Alshomrani, A.S. Observer-based memory consensus for nonlinear multi-agent systems with output quantization and Markov switching topologies. *Phys. A Stat. Mech. Its Appl.* **2020**, *551*, 123949. [CrossRef]
21. Sakthivel, R.; Parivallal, A.; Huy Tuan, N.; Manickavalli, S. Nonfragile control design for consensus of semi-Markov jumping multiagent systems with disturbances. *Int. J. Adapt. Control. Signal Process.* **2021**, *35*, 1039–1061. [CrossRef]
22. Polloni, L.; Mati, R.; Innocenti, M.; Campa, G.; Napolitano, M. A Synthetic Environment for the Simulation of Visionbased Formation Flight. In Proceedings of the AIAA Modeling and Simulation Technologies Conference, Austin, TX, USA, 11–14 August 2003.
23. Ray, R.; Cobleigh, B.; Vachon, M.; St John, C. Flight Test Techniques used to Evaluate Performance Benefits During Formation Flight. In Proceedings of the AIAA Atmospheric Flight Mechanics Conference and Exhibit, Monterey, CA, USA, 5–8 August 2002.
24. Seanor, B.; Campa, G.; Gu, Y.; Napolitano, M.; Rowe, L.; Perhinschi, M. Formation Flight Test Results for UAV Research Aircraft Models. In Proceedings of the AIAA 1st Intelligent Systems Technical Conference, Chicago, IL, USA, 20–22 September 2004.
25. Sattigeri, R.; Calise, A.; Kim, B.S.; Volyanskyy, K.; Kim, N. 6-DOF Nonlinear Simulation of Vision-Based Formation Flight. In Proceedings of the AIAA Guidance, Navigation, and Control Conference and Exhibit, San Francisco, CA, USA, 15–18 August 2005.
26. Lin, J.; Miao, Z.; Zhong, H.; Peng, W.; Wang, Y.; Fierro, R. Adaptive Image-Based Leader-Follower Formation Control of Mobile Robots with Visibility Constraints. *IEEE Trans. Ind. Electron.* **2021**, *68*, 6010–6019. [CrossRef]
27. Chen, X.; Jia, Y. Adaptive leader-follower formation control of nonholonomic mobile robots using active vision. *IET Control. Theory Appl.* **2015**, *8*, 1302–1311. [CrossRef]
28. Sattigeri, R.; Calise, A.J.; Evers, J.H. An adaptive vision-based approach to decentralized formation control. *J. Aerosp. Comput. Inf. Commun.* **2004**, *1*, 502–525. [CrossRef]
29. Chen, Q.; Jin, Y.; Wang, T.; Wang, Y.; Yan, T.; Long, Y. UAV Formation Control Under Communication Constraints Based on Distributed Model Predictive Control. *IEEE Access* **2022**, *2022*, 126494–126507.
30. Qin, J.; Zhang, G.; Zheng, W.X.; Kang, Y. Adaptive Sliding Mode Consensus Tracking for Second-Order Nonlinear Multiagent Systems with Actuator Faults. *IEEE Trans. Cybern.* **2019**, *49*, 1605–1615. [CrossRef]
31. Desai, J.P.; Ostrowski, J.; Kumar, V. Controlling formations of multiple mobile robots. In Proceedings of the IEEE Transactions on Robotics & Automation, Leuven, Belgium, 20 May 2010; Volume 6, pp. 905–908.
32. Das, A.K.; Fierro, R.; Kumar, V.; Ostrowski, J.P.; Spletzer, J.; Taylor, C.J. A vision-based formation control framework. *IEEE Trans. Robot. Autom.* **2002**, *18*, 813–825. [CrossRef]
33. Mariottini, G.L.; Morbidi, F.; Prattichizzo, D.; Vander Valk, N.; Michael, N.; Pappas, G.; Daniilidis, K. Vision-Based Localization for Leader-Follower Formation Control. *IEEE Trans. Robot.* **2009**, *25*, 1431–1438. [CrossRef]
34. Galzi, D.; Shtessel, Y. UAV formations control using high order sliding modes. In Proceedings of the American Control Conference, Minneapolis, MN, USA, 14–16 June 2006.

35. Kadungoth Sreeraj, A.R. A Model-Free Control Algorithm Based on the Sliding Mode Control Method with Applications to Unmanned Aircraft Systems. Ph.D. Thesis, Rochester Institute of Technology, Rochester, NY, USA, 2019.

36. Mobayen, S. Adaptive Global Terminal Sliding Mode Control Scheme with Improved Dynamic Surface for Uncertain Nonlinear Systems. *Int. J. Control. Autom. Syst.* **2018**, *16*, 1692–1700. [CrossRef]

37. Dehghani, M.A.; Menhaj, M.B. Integral sliding mode formation control of fixed-wing unmanned aircraft using seeker as a relative measurement system. *Aerosp. Sci. Technol.* **2016**, *58*, 318–327. [CrossRef]

38. Ailon, A.; Zohar, I. Controllers for trajectory tracking and string-like formation in Wheeled Mobile Robots with bounded inputs. In Proceedings of the Melecon 2010–2010 15th IEEE Mediterranean Electrotechnical Conference, Valletta, Malta, 26–28 April 2010.